Displacement and strain estimation for evaluation of arterial wall stiffness using a familial hypercholesterolemia swine model of atherosclerosis

Wenqi Ge
Department of Medical Physics and Department of Electrical and Computer Engineering, University of Wisconsin, Madison, Wisconsin 53705

Christian G. Krueger, Ashley Weichmann, and Dhanansayan Shanmuganayagam
Reed Research Group, Department of Animal Science, University of Wisconsin, Madison, Wisconsin 53705

Tomy Varghese[a)]
Department of Medical Physics and Department of Electrical and Computer Engineering, University of Wisconsin, Madison, Wisconsin 53705

(Received 28 January 2012; revised 27 April 2012; accepted for publication 9 May 2012; published 2 July 2012)

Purpose: To track variations in the deformation of the arterial wall noninvasively by estimating the accumulated displacement and strain over a cardiac cycle may provide useful indicators of vascular health.
Methods: In this paper, we propose an approach to track a region of interest (ROI) locally and estimate arterial stiffness variation in a familial hypercholesterolemic swine model of spontaneous atherosclerosis that allows for systematic and reproducible study of progression of the disease mechanism.
Results: Strain and displacement indices may be derived from the variations of the accumulated displacement and accumulated strain (obtained from the gradient of the accumulated displacement) over a cardiac cycle to predict not only the likelihood of developing vascular diseases, but also the sites where they may occur. Currently, an ROI thickness value of less than one mm within the arterial wall is necessary for the axial accumulated displacement and strain to obtain reproducible estimates.
Conclusions: Accumulated axial displacement and strain estimation on the artery wall shown in this paper indicate the repeatability of these measurements over several cardiac cycles and over five familial hypercholesterolemic swine. Our results also demonstrate the need for a small region of interest within the arterial walls for accurate and robust estimates of arterial function. © *2012 American Association of Physicists in Medicine*. [http://dx.doi.org/10.1118/1.4722746]

Key words: ultrasound, elastography, atherosclerosis, arterial wall stiffness

I. INTRODUCTION

The leading cause of death in the United States are cardiovascular diseases (CVD).[1] In 2007, one out of every 2.9 deaths in the United States was attributed to cardiovascular disease.[2] Over 1.2 million Americans were estimated to have suffered coronary events and about 795 thousand suffered strokes.[2] Measurements of arterial stiffness are useful for identifying those with higher cardiovascular risk factors attributed to a wide range of characteristics, including age, gender, obesity, hypertension, and genetic factors.[3] In addition, arterial stiffness can be used to detect various cardiovascular complications such as left ventricular hypertrophy and failure, aneurysm formation and rupture, and atherosclerosis, which can lead to stroke, myocardial infarction, and renal failure.[4,5]

Furthermore, the younger population in the United States is increasingly at risk for CVD, because of the increased prevalence of childhood obesity, metabolic syndrome, diabetes, etc.[2,6] These increased risks warrant preventive and interventional measures be taken at earlier stages of disease progression. Early detection of CVD is therefore essential and noninvasive methods for imaging and measuring arterial stiffness, as described in this paper, may provide new potential diagnostic information.

Measurement of the pulse-wave velocity (PWV) is the prevalent method for noninvasively quantifying arterial stiffness and identifying cardiovascular risk factors.[3,7,8] The Moens-Korteweg equation shows that the PWV is related to the square root of vessel stiffness

$$\mathrm{PWV} = \sqrt{((E * h)/(2r\rho))}, \tag{1}$$

where E is the Young's modulus, h is the vessel wall thickness, r is the vessel radius, and ρ is the blood density.[4,7] PWV is measured using the pulse transit time (PTT), calculated from the foot-to-foot or wave front to wave front time delay between two arterial sites divided over the separation distance.[4,7,9] PWV can be meaningfully measured at multiple locations in the body. For example, the brachial-ankle PWV has been shown to be an indicator of atherosclerosis[10] and the aortic PWV and carotid-femoral PWV (cfPWV) has been shown to be predictive of cardiovascular events.[8,9] PWV has numerous drawbacks. First, PWV measurements of upper limb muscular arteries do not change significantly with age.[4] Since PWV measurements characterize a length of vessel, they cannot be localized to any specific point.[11] Furthermore, effectiveness of PWV measurements can be affected by the traveled medium, such as muscular arteries, which have

a different stiffness than elastic arteries.[10] Depending on the site and methodology of the measurement, finding the PWV can also be inconvenient; the pressure sensitive transducers used to measure carotid and femoral PWV requires training and could take more than 20 minutes.[10] Recent methods of PWV measurement were shown to be viable for finding measurements in regions on the order of tens of millimeters.[12,13] Despite the increased ease of acquisition and precision in the lateral direction, PWV's largest weakness is that the measurement is confined to the temporal and lateral domains. It cannot be used to find varying stiffness among the layers of the arterial wall. Strain estimation does not suffer from the aforementioned issues and can be used to supplement existing methods for diagnosis and risk assessment.

Measurement of the carotid intima-media thickness (CIMT) is another indicator of atherosclerosis and predictor of coronary artery diseases.[14] It has been shown to predict cardiovascular diseases independent of traditional risk factors such as coronary artery calcium (CAC), smoking, hypertension, diabetes, fibrinogen, and LDL cholesterol.[15–17] CIMT is measured using high resolution ultrasound B mode images and can be used in conjunction with elastography based measurements of arterial stiffness.

Elastography is a method of creating images that map tissue stiffness.[18] In classical external compression elastography, strain tensors are estimated from local displacements caused by quasi-static uniaxial externally applied deformations.[18–20] Local displacements are usually tracked and estimated using 2D cross-correlation based methods described in the current literature.[19,21–23] After correcting for the applied stress and using the appropriate boundary conditions, the displacement/strain images can be used to calculate the elastic modulus map.[18] The classical analogy of elastography is palpation, where manual pressure is applied by a medical practitioner to sense the position, stiffness, mobility, and pulsation of internal structures.[24] Strain is defined as the deformation per unit length in percentage of an object under stress and the normal strain is defined as

$$\varepsilon_{zz} = \partial u_z / \partial z, \tag{2}$$

$$\varepsilon_{yy} = \partial u_y / \partial y, \tag{3}$$

where u is the displacement in the direction of the strain and z and y are the coordinates in the axial and lateral directions.

Elastography has been utilized for vessel wall characterization and assessment of atherosclerotic plaque, utilizing the internal deformation of the vessel generated by blood-flow.[25–28] Subsequent studies using acoustic radiation force impulse imaging (ARFI) have shown the ability to identify the presence of and discriminate between hard and soft plaques.[29–31]

A study using hypercholesterolemic and normocholestrolemic swine also showed the effectiveness to materially characterize atherosclerotic plaque.[32] Currently, elastography is accepted as a safe, noninvasive, patient-friendly, and inexpensive method of imaging tissue stiffness and can help diagnose cancer, identify atherosclerosis, and monitor ablation.[19,24,33] Elastography has the ability to locally characterize the elastic properties of arterial wall along the dimensions of time and space with precision.

Previously, Shi *et al.*[25] utilized the accumulated axial strain variation to compute the maximum accumulated axial strain and relative lateral shift as indices for the differentiation of calcified plaque from soft plaque in human subjects. Variations in the accumulated strain within a specified region of interest (ROI) in plaque tissue with dimensions of 64 points in the axial direction and 5 lines in the lateral direction were utilized. Strain estimates within the ROI were averaged and their values summed to produce their accumulated strain. The accumulated strain used in this paper is generated by accumulating the displacement over time within the ROI. The resulting accumulated displacement is then summed point by point over the cardiac cycle, which is then utilized to obtain the accumulated strain curve. Effectively, if local strain is defined by the expression, $\varepsilon_{zz} = \partial u_z / \partial z$, the accumulated axial strain as defined in this paper is given by

$$\alpha_{zz} = \partial V_z / \partial z, \tag{4}$$

$$V_z = \frac{1}{n} \sum u_z, \tag{5}$$

where V_z denotes the accumulated displacement over the cardiac cycle.

In this paper, we propose a method where the local strain distribution in an ROI in the arterial wall of a familial hypercholesterolemic (FH) swine model is monitored over time by acquiring and processing a time series of ultrasound radio frequency (RF) echo-signal frames. The FH swine is a unique validated animal model of spontaneous atherosclerosis that allows for systematic and reproducible study of disease mechanism and testing of emerging diagnostic and therapeutic ultrasound technologies.[34–36] The FH swine is the only large animal model that develops spontaneous atherosclerotic lesions when fed with a normal diet without added cholesterol.[37–40] The FH swine, with its genetic proximity to human[41] and similarities in cardiovascular pathophysiology (atherogenesis, coronary artery disease, and ischemia), lipoprotein metabolism, digestive physiology, and dietary adaptations, makes it an excellent translational model for longitudinal studies of vascular biology.[42–44]

We utilize accumulated strain estimates calculated from the accumulated displacement over an ROI. The ROI is operator defined and the deformation of the region is tracked over multiple cardiac cycles. We address estimation of the axial and lateral displacement vectors and strain using backscattered ultrasound signals. The maximum accumulated axial strain and the maximum accumulated lateral displacement have been utilized as indices to characterize plaque.[25] We propose to utilize these indices for characterizing arterial stiffness as also discussed next in this paper.

II. MATERIALS AND METHODS

The strain distribution within a vessel wall over a cardiac cycle may provide useful information indicative of age related

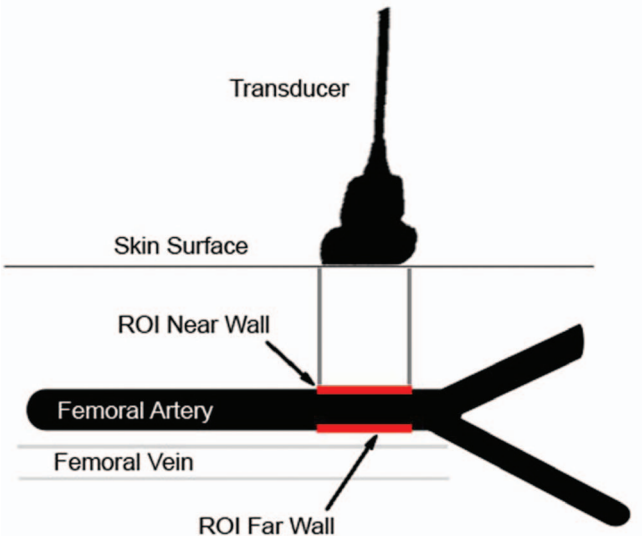

FIG. 1. Schematic diagram of the region of the femoral artery that was imaged on the FH swine model of atherosclerosis.

arterial stiffening and cardiovascular health. An ROI is defined in the artery near and far walls that would exclusively lie within the wall of the blood vessel. Figure 1 provides a schematic diagram of the ultrasound scan performed along with identification of the ROI location using an FH swine model of atherosclerosis. As the vessel expands and contracts over the cardiac cycle, the ROI changes its shape and location correspondingly. This allows for the capture of a displacement/strain profile of the vessel wall over the cardiac cycle instead of just a snapshot in time.

At 6 weeks of age (2 weeks postweaning), the five female FH swine were placed on a corn–soybean mixed diet with 2% added fat, and fed twice daily. The daily calorie intake was limited to 80% of *ad libitum* intake (based on *ad libitum* intake of age-matched FH swine). The diet was formulated to meet nutrient requirements, and was mixed weekly from feed components (Arlington Feed Mill, Arlington, WI). At the time of the ultrasound measurements, the animals were 10.6 ± 0.5 months old, with a body weight of 83.6 ± 6.9 kg (24.6 ± 4.8% body fat, determined by dual energy x-ray absorptiometry). A midline neck incision was made to access the internal carotid artery. A catheter was placed in the artery for intra-arterial blood pressure (ABP) measurement via an attached pressure transducer (PX600 Edwards Lifesciences, Irvine, CA), positioned at the level of the heart and connected to an S/5 Datex-Ohmeda Anesthesia Monitoring System (GE Healthcare, Waukesha, WI). ABP and heart rate measurements for the 5 FH swine are shown in Table I.

TABLE I. Intra-arterial blood pressure (BP) and heart rate measurements for the five FH swine.

Animal no.	Systolic BP	Diastolic BP	Heart rate
1	75	38	140
2	77	46	153
3	79	40	105
4	88	40	110
5	82	46	94

II.A. Radio frequency data acquisition

Acquisition of the RF data was accomplished using the clinical Ultrasonix SonicTouch system (Ultrasonix Medical Corporation; Richmond, BC) running Sonix RP 3.1.9, and using an L14-5/38 transducer operating at 10 MHz center frequency. The depth of the RF data acquired, measured from the transducer to the vessel, was 40 mm. The sampling frequency for the acquired data was 40 MHz with a frame rate of 98 frames/s.

Ultrasound scanning was performed on the FH swine model starting at six months of age. This study was performed under a protocol approved by the University of Wisconsin-Madison Animal Care and Use Committee (ACUC). The animals were sedated once per month with an injection of Telazol at 1–5 mg/kg, at the minimal dosage necessary for sedation prior to the use of a facemask. The facemask then delivered 1.5%–5% isoflurane and 100% oxygen with a flow rate of 1–3 L/min. Heart monitor and oxygen saturation were monitored via pulse oximetery. After sedation, the ultrasound transducers were held by hand to initiate scans that lasted for one or more cardiac cycles. The field of view included the femoral artery and the beginning of the bulb with a single focus at the far wall of the vessel. Atherosclerosis is a systemic disease; therefore, plaque accumulation is expected to occur at multiple arterial locations. The femoral artery was chosen due to the presence of a bifurcation site where atherosclerotic plaques tend to develop, and is much easier to access using ultrasound than the carotid artery in swine due to the difference in imaging depths.

II.B. Strain and displacement mapping

The 2D displacement tracking and strain estimation algorithm was implemented in MATLAB (The Mathworks, Natick, RI). The code used to calculate the displacement was an implementation of the quality-guided displacement tracking algorithm.[45] This multi-seed algorithm initially utilizes regularly spaced windows as initial seeds. Cross correlation coefficients between the tracked regions and the seeds were used to determine the quality of each seed, and the highest one would be selected to be the initial estimation of displacement. The algorithm then iterates to track the seed's four neighbors and the process repeats for the next windows to complete the entire scanned field. A large window size allows for better tracking of noisy data while a smaller window improves spatial resolution.

RF data sets were upsampled by a factor of 5 using spline interpolation to improve displacement tracking. The dimensions of the 2D motion tracking kernel were 81 data points along the beam direction and 15 data points along the lateral direction for the upsampled data, corresponding to 0.33 mm $\times$ 0.88 mm for the 2D tracking kernel dimensions, respectively. A 75% overlap was utilized to obtain consecutive displacement estimates. Local strain estimates were obtained using a least squares fit to the displacement data using

segments with a length of 0.66 mm for the axial strain estimates and 0.88 mm for the lateral strain estimates. The frame skip amount, which represents the number of frames that were skipped to ensure a reasonably significant amount of deformation between frames, was set to 3. By increasing the amount of displacement between consecutively processed frames, the signal to quantization noise ratio and the subpixel displacement estimation errors were improved. Before the displacement maps were used to calculate the local strain images, they were put through a 3×2 pixel median filter to remove noise spikes. Displacements and strains estimated along the x (lateral) and y (axial) directions along with the strain distribution are stored for every frame-pair for further processing. The accumulated displacement was then computed from the stored displacement estimates. Lastly, the accumulated strain was computed from the accumulated displacement, estimated over the cardiac cycle.

II.C. ROI creation and tracking

The positioning of the ROI on the artery wall was determined manually for the first frame and their coordinates were adjusted using previously calculated displacements for the following frames. The ROI boundary was defined using points marked along the vessel intima on the first frame of the RF data and extended from the beginning of the bifurcation toward the common femoral artery. The lines that connect neighboring points were used to create the defining curved edge of the ROI, and the ROI region is delineated according to the contours of this edge. The opposite edge was created by translating the defining edge up or down by the intended thickness of the ROI, resulting in an area that has uniform thickness. The resulting ROI was uniform in thickness. For example, on the near wall of an artery, points should be marked directly below and adjacent to the vessel wall, and the ROI would be defined to extend a set number of pixels above the defining edge to cover the wall and some of the surrounding tissue; the inverse holds true for the far wall. This assured a uniform thickness for the initial ROI. This method is valid only with the assumption that the ROI is intended for an object that is horizontally situated, otherwise it would be necessary to define the ROI width and height at different angles from the RF data's cardinal directions. An ROI maximum length can optionally be defined, and any region that extend above the set length would be cut off. It is advantageous to use ROIs that are larger than what is required so that data can be easily derived as a subregion of the processed data. Care should therefore be made to mark the ROI with a starting point on either the left or right side that is anatomically similar across different data sets. The ROI dimensions used for the swine data were 10 mm in width and up to 3 mm in thickness or depth; the actual thickness used for processing was about one mm in thickness to correspond to and to lie within the actual thickness of the vessel walls.

The data points that make up the defining edge of the near wall and the far walls of the corresponding ROI were each tracked over the cardiac cycle and the ROI was redrawn for each subsequent frame based on this information. The displacement calculated from the RF data with coordinates in space and time was added to the coordinates of the points of the ROI's defining edge to form the ROI of the next frame in time. The stored coordinates for the ROI edge were not integers since subsample displacements were estimated. Bilinear interpolation was used to find the displacement values for the next frame. This reduces the rounding errors that can be significant in the lateral direction as discussed in the Appendix.

Once the ROI was generated, the strain, displacement, and any other relevant data points within the corresponding region can be stored. First the ROI is made into a binary mask, with ones corresponding to pixels within the ROI and zeroes otherwise. Then mask can then be applied to the strain and displacement images. Since the initial ROI points were marked at the exact boundary between the vessel and the blood within it to remove the contribution of the blood in the strain image. The ROI follows the curvature of the vessel wall and is not discarded. The ROI thickness is specified in the number of displacement/strain pixels used to estimate the displacement and strain. The two dimensions are therefore the location on the vessel wall and the ROI thickness within the vessel wall. The strain and displacement maps can be saved directly as a result of the mask, and the accumulated strain and accumulated displacement maps can be found after accumulating the displacements.

III. RESULTS

Figure 2(a) presents the B-mode image of the femoral artery being scanned on the FH swine. The location of the scan is relative to the femoral artery's bifurcation on the B-mode image. The local displacement maps estimated along the axial (b) and lateral (c) directions are also shown along the corresponding axial (d) and lateral (e) strain distribution. Noise artifacts in the lateral displacement and strain images are increased when compared to the axial displacement and strain images, respectively. The locations of the ROI around the near and far walls of the artery are illustrated in Fig. 3(a), on the ultrasound B-mode image. The ROIs are delineated manually on the B-mode image with the lumen of the artery identified in both the near and far walls of the artery. The ROI over which local displacement and strain estimates are estimated and accumulated should ideally be marked individually on ultrasound B-mode images rather than the derived strain image. This can be done very accurately using image software such as MITK 3M3 program (Mint Medical GmbH, Heidelberg, Germany) to measure the B-mode vessel thickness. Estimations are performed using the B-mode images by determining the edges of the vessel wall and using the ratio of the pixels making up the vessel thickness over the pixel height of the image multiplied by the corresponding image depth. The resulting vessel thickness obtained is on the order of 0.8–0.72 mm. On the other hand the thickness of the femoral artery obtained from a representative histopathological image in Fig. 3(b), instead shows the vessel thickness to be around 0.3–0.4 mm.

The near wall of the artery is constrained by surrounding connective tissue, subcutaneous fat, and the skin. Since the

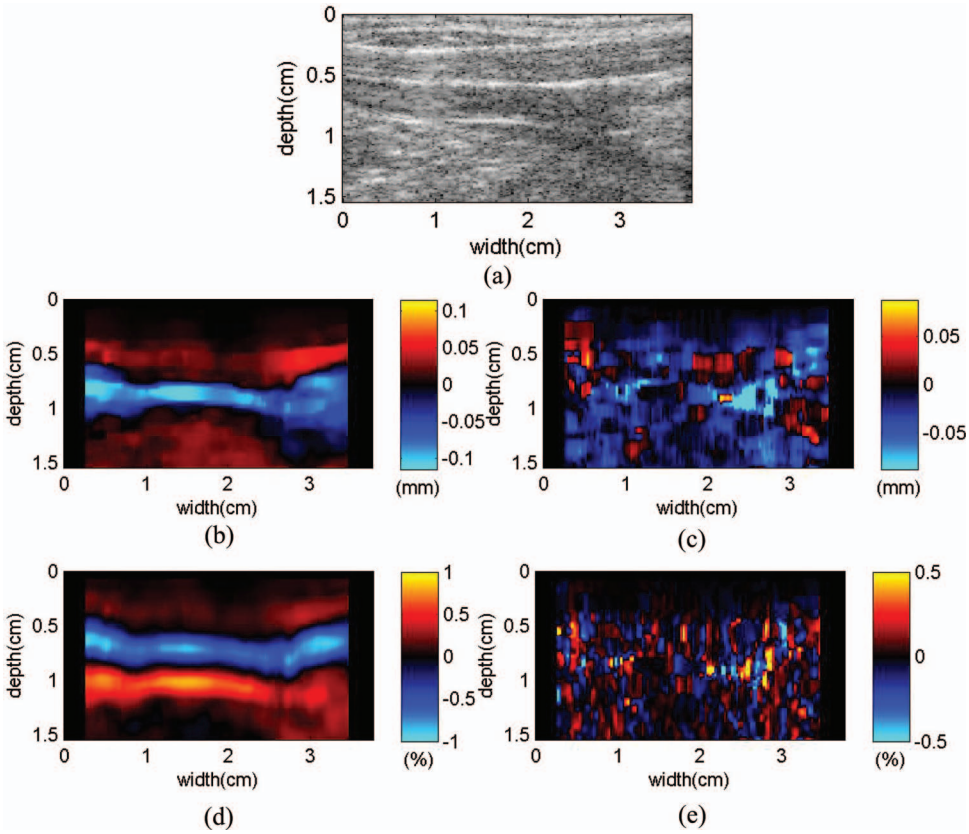

FIG. 2. Ultrasound B-mode image (a), the accumulated axial displacement (b), the accumulated lateral displacement (c), the corresponding accumulated axial strain (d), and lateral strain images over a cardiac cycle (e).

transducer is placed next to the skin layer, the near wall of the artery is not expected to deform significantly with blood flow. On the other hand, the far wall of the artery is mainly constrained by connective tissue, a vein that runs along with the artery and is visible in the B-mode image and muscle tissue. The far wall therefore usually deforms more than the near wall of the artery in the geometry shown in Figs. 2 and 3. Local displacements and strains within these ROIs are utilized in the following plots to evaluate arterial stiffness variations.

Figure 4 presents the variation of a single row of displacement and strain estimated along the inner boundaries of the ROI that are closest to the vessel wall lumen. We track the displacement of these points that are drawn manually on the first B-mode images over all the RF data acquired over the cardiac cycle. Since this row of data points will move along with the arterial wall and track the deformation introduced in a cardiac cycle, we refer to the estimation presented in Fig. 4, as the localized displacement and strain, since we track the same tissue structure over the entire cardiac cycle. Observe the opposite directions of the periodic displacement visualized on the near and far wall for the axial accumulated displacement (AAD), and the noisier variation for the axial accumulated strain (AAS). A periodic trend in the AAS can, however, be visualized. A phase lag between the AAD of the near and far wall is also observed. Although the lateral accumulated displacements (LAD) indicate the arterial deformation along the lateral direction, the lateral accumulated strains (LAS) do not present a trend and are extremely noisy estimates. The displacement and strain values of the near wall are usually lower in magnitude when compared to the far wall. This could be due to location's proximity to the transducer and the proximity of the scanned artery to the femoral vein.

We now include additional displacement and strain estimates by increasing the thickness of the ROI to 1 mm, with the plots for the near and far wall shown in Fig. 5. The AAD and AAS curves are similar to those observed in Fig. 4, while the LAD curve being slightly lower. The LAS curves are still noisy and we will not discuss the variations associated with this curve from this point forward due to the increased noise artifacts observed.

To clearly visualize the trend or variations in the mean of the AAS curves, we replace the standard deviation with the standard error in Fig. 6. We present plots of the near and far wall for different ROI thicknesses in Fig. 6. Note that for ROI thickness of a single strain estimate (0.69 mm) in Fig. 6(a), 2 estimates (0.79 mm), 4 estimates (1 mm), and 10 estimates (1.48 mm) in Figs. 6(b)–6(d), respectively. Note that as the ROI thickness becomes larger it also incorporates estimates from surrounding overlying tissue which contrast from the strain in arterial tissue as seen in Fig. 6(d). Appropriate selection of the dimensions of the ROIs and a fine resolution are essential to properly characterize variations in arterial elasticity.

Figures 7 and 8 present the changes in the accumulated axial and lateral displacements and strains around the peak and valley of the axial deformations over the cardiac cycle

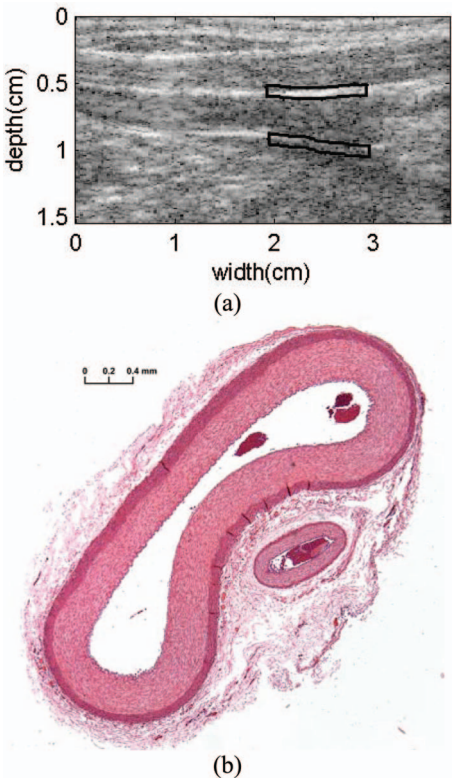

FIG. 3. (a) Ultrasound B-mode image with the regions of interest on the near wall and the far wall of the femoral artery and (b) representative photomicrograph (5× objective) of a hematoxylin and eosin stained cross section of a femoral artery from an 8-month-old FH swine.

at approximately 0.35 and 0.89 s into the cardiac cycle. Estimated displacements are interpolated to provide similar pixel density as the underlying ultrasound radio frequency data for accurate registration. The strain is maximum on the interior of the vessel, progressing to a zero point and ultimately to surrounding tissues with the opposite sign. Larger ROI thickness enables us to evaluate stiffness variations in tissues surrounding the vessel. Note that accurate and robust estimates of arterial function are obtained for ROI thickness values less than 1 mm for the axial accumulated displacement and strain and less than 0.5 mm for the lateral accumulated displacements. The lateral accumulated strains are shown but the estimates are rather noisy.

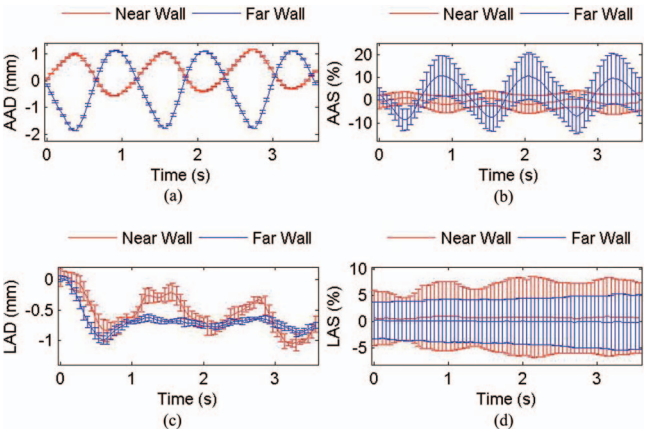

FIG. 4. Plots of the accumulated axial displacement (a) and strain (b) and the accumulated lateral displacement (c) and strain (d) shown over two cardiac cycles and computed over a region of interest that is 0.63 mm in thickness or a single row of strain estimates and 1 cm in length. The error bars denote the standard deviation for data points with the 1 mm ROI from the surface of the artery that are tracked over the cardiac cycle for both the near and far wall.

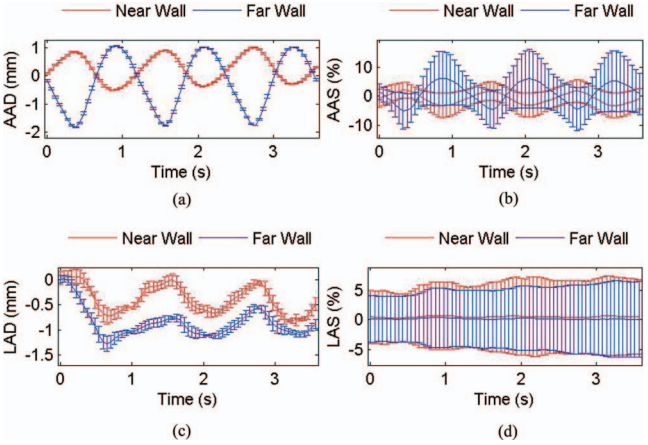

FIG. 5. Plots of the accumulated axial displacement (a) and strain (b) and the accumulated lateral displacement (c) and strain (d) shown over two cardiac cycles and computed over a region of interest that is 1 mm in thickness and 1 cm in length. The error bars denote the standard deviation for data points with the 1 mm ROI from the surface of the artery that are tracked over the cardiac cycle for both the near and far walls.

Figure 9 shows the progression of strain away from the vessel walls. The decaying shape of the far wall agrees with the simulated strain of the mathematical vessel model put forth by Maurice *et al.*[27] and the phantom model by Korte *et al.*[46] made using a phantom with an inner lumen tube of 4 mm diameter and outer vessel tube of 15 mm diameter, with soft gelatinous material filling in between. The edge of the vessel wall exhibits a region of slower decay which is likely to show a difference between the intima media and adventitia. In addition, the near wall clearly exhibits a different strain curve than the far wall. The curve does not appear to be an

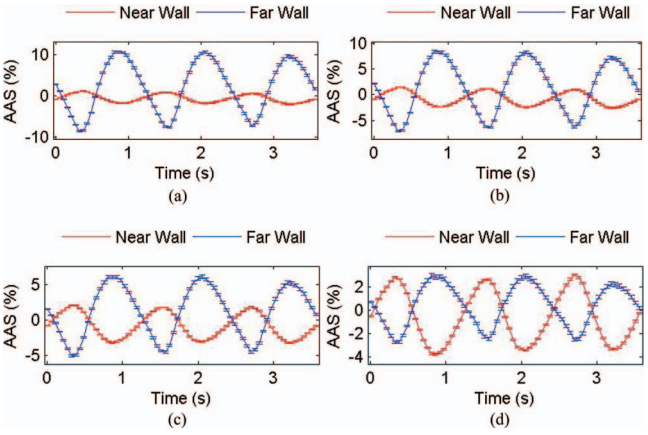

FIG. 6. Plots of the accumulated axial strain for an ROI with a thickness of one row (a), along with the corresponding curves for an ROI with a 0.79 mm thickness (b), 1 mm thickness (c), and 1.48 mm thickness (d). The error bars in this figure denote the standard error to clearly indicate the strain variations in the near and far wall.

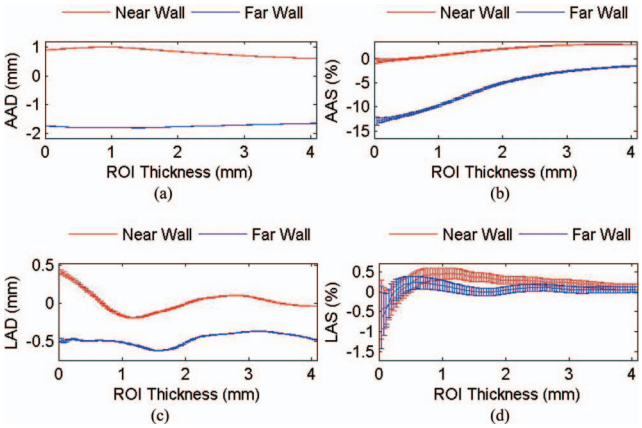

FIG. 7. Plots of the accumulated axial displacement (a) and strain (b) and corresponding lateral displacement (c) and strain (d) versus ROI thickness. Values are plotted at the peak of the cyclic curves shown in Figs. 4–6 or at a time instant of approximately 0.35 s into the cardiac cycle. The error bars in this figure denote the standard error to clearly indicate mean variations in the near and far wall.

artifact, since the curve is consistent from one cardiac cycle to the next and transitions between the two waveforms shown in Figs. 9(c) and 9(d). This illustrates that the vessel strain is not uniform in neither the radial nor the circumferential directions and could exhibit very different characteristics warranting further examinations. The vessel wall thickness of a healthy swine is between 0.3 mm and 0.5 mm, and the intima media can progress to twice its thickness in less than a year with plaque accumulation.[35] The human carotid artery is thicker, on the order of 0.5–0.8 mm in healthy human male subjects according to a 1996 study.[47] However, stretching and thickening of the arterial wall occur during the cardiac cycle, which may also increase the imaged thickness of the vascular arterial wall. The current displacement tracking and strain processing kernels are on the order of the vessel thickness, however, the resolution is improved due to the overlapping kernels used for strain estimation.

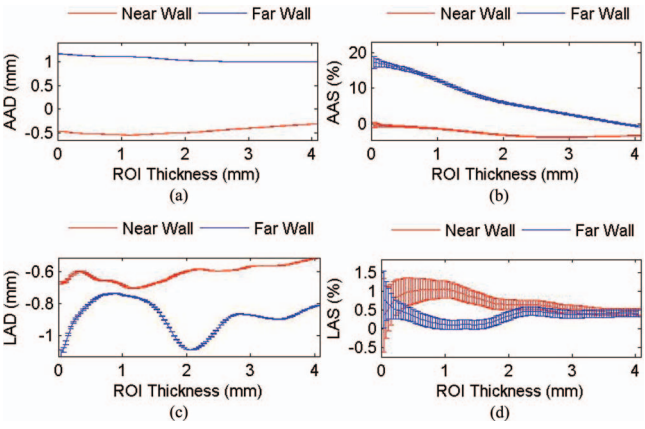

FIG. 8. Plots of the accumulated axial displacement (a) and strain (b) and corresponding lateral displacement (c) and strain (d) versus ROI thickness. Values are plotted at the valley of the cyclic curves shown in Figs. 4–6 or at a time instant of approximately 0.89 s into the cardiac cycle. The error bars in this figure denote the standard error to clearly indicate mean variations in the near and far wall.

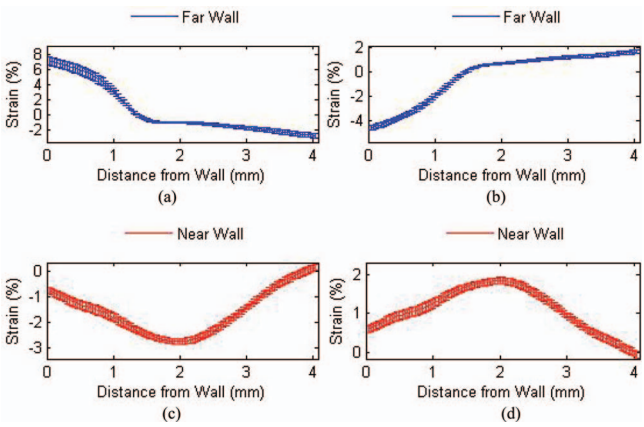

FIG. 9. Plots showing the average axial strain of a single row of pixels versus their distance from the far wall (a, b) and the near wall (c, d) at their peaks during the cardiac cycle. The values remain consistent from one cardiac cycle to the next. The error bars in this figure denote the standard error to clearly indicate mean variations in the near and far walls.

Figure 10 shows the accumulated axial displacement and accumulated axial strain curves for five FH swine. The plots are normalized in both time to two cardiac cycles and amplitude to the systolic blood pressure of each model respectively. The normalization is done frame by frame. For each frame of the far wall displacement, the mean value is calculated for an ROI of 0.6 mm depth and the peak to peak change is computed. The accumulated displacement for the near and far walls are scaled by dividing by this value. The scaled accumulated displacement map is then used to calculate the accumulated strain. The amplitude of the plots contain strain and displacement contributions of tissue outside the vessel wall due to the thickness of the ROI, but the curvature of the vessel wall is maintained. The plots show the repeatability of

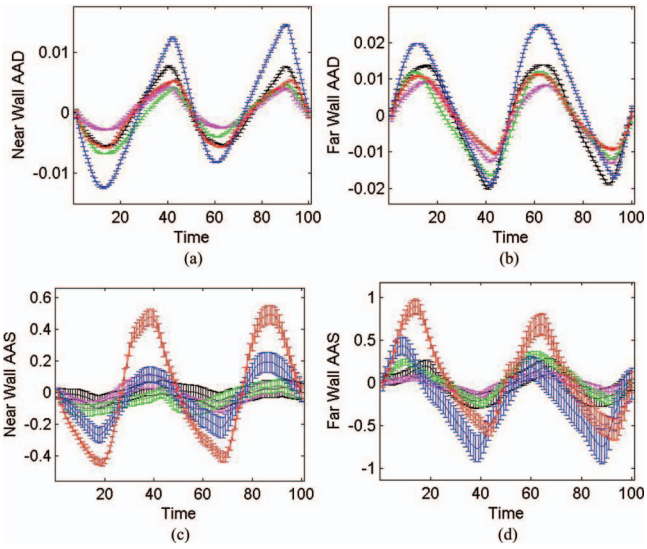

FIG. 10. Plots showing accumulated axial displacement of the near and far wall (a, b) and the accumulated axial strain of the near and far wall (c, d) for five FH swine. Plots are shown for ROI with 0.6 mm thickness. Normalization was performed by dividing the amplitudes of the near and far wall displacements by the systolic blood pressure. The axes are both unit-less due to the normalizations. The error bars in this figure denote the standard error to clearly indicate mean variations in the near and far walls.

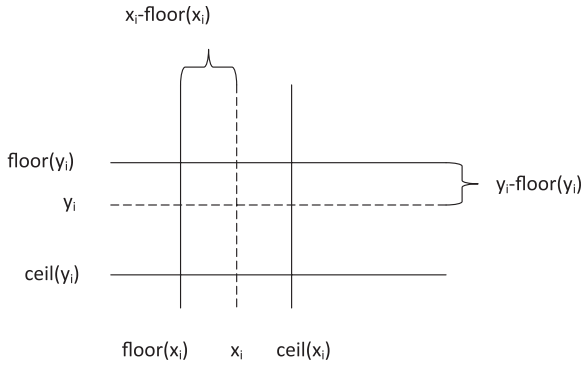

FIG. 11. Diagram showing the coordinate grid used for bilinear interpolation. When a data point is located at a noninteger coordinate, the data points located at the four neighboring integer coordinates, found via rounding, are used for the estimation of the value at that location.

our displacement tracking and strain estimation approach, and also the variability between the FH swine. Table I provides the blood pressure and heart rate information that was used in the normalization, for each FH swine.

IV. DISCUSSION

In this paper we demonstrate the ability to accurately track local displacements on either sides of the lumen of an artery wall. The deformation of the artery wall within the cardiac cycle is expected to change with age with the stiffening of the arteries due to atherosclerosis. The FH swine model used in this paper can be used to, track arterial stiffening for animal with different diets and over age ranges. The noninvasive arterial stiffening data obtained with strain imaging can be correlated to histopathological assessments on the artery after the animal is sacrificed.

Several features or indices can be derived from the variation in the AAD, AAS, and LAD plots shown in this paper. The more obvious features include the variations in the maximum and minimum mean and standard deviations of the AAD, AAS, and LAD estimates, shown in Figs. 7 and 8 over different animals. The phase difference or lag between the AAD, AAS, and LAD variations between the near and far walls of the artery would be another feature that would provide important information. The slope of the increase of the AAD, AAS, and LAD curves during systole and the subsequent decrease during diastole will also be tracked across a subgroup of these animals.

The axial displacement and strain estimation on the artery wall shown in this paper indicate the repeatability of these measurements over several cardiac cycles as illustrated in Figs. 4–6. The larger dimensions or thickness of the ROI include contributions from tissue surrounding the artery wall such as connective tissue, subcutaneous fat or muscle tissue. The localized estimation of the displacement and strain in Fig. 4, with the ROI that tracks the movement of the lumen would provide the most consistent results, and larger ROIs should be compared to the estimates to ensure that the ROI remains within the arterial wall. Larger ROIs may reduce the statistical fluctuation of the results since more independent estimates are included in the computation of the mean and standard deviation.

V. CONCLUSIONS

Currently, the strain distribution is predominantly used to find scalar values, be it the maximum, minimum, or the mean strain within a region. By tracking arterial wall tissue as it deforms over time, strain can be seen as a multidimensional matrix, not only in space, but also in time. By localizing strain onto an area of tissue, i.e., the arterial wall, it may be possible to predict the likelihood of developing vascular diseases, the nature and progression of the cardiovascular system, and the sites where they may occur.

Preliminary results demonstrated the feasibility of obtaining the required data. Further improvements can be made to the tracking accuracy, especially in the lateral direction, and improved definition of the data in the axial direction, which could potentially indicate individually the health of the media and adventitial layers. The assumption of the ROI's uniform thickness could be discarded for a mesh tracking approach, that allow for much higher precision in tissue tracking. The biggest difficulty of tracking using ultrasound is the poor resolution and sampling in the lateral direction. Methods such as beam steering and improved subpixel estimation may bring further improvements in this aspect. The accumulated strain as defined in this paper will be explored for its potential for noninvasive characterization of the vascular wall.

ACKNOWLEDGMENTS

This research was supported in part by NIH Grant Nos. R21 EB010098-03, R01 CA112192-S103 and the Reed Research Group Multi-Donor Fund (UW-Madison).

APPENDIX: SUB-SAMPLE DISPLACEMENT TRACKING

Bilinear interpolation was used in the process of incrementing the ROI coordinates as described below and shown schematically in Fig. 11. Let nonintegers x_i and y_i denote the coordinates of a point in the ROI boundary with subscript index, i, representing time; let $dy(x_i, y_i)$ be the displacement estimate located at (x_i, y_i), and f and c correspond to the floor and ceil functions (round up and round down functions) respectively, then

$$x_{i+1} = x_i + dx(f(x_i),\ f(y_i))\frac{(c(x_i)-x_i)(c(y_i)-y_i)}{(c(x_i)-f(x_i))(c(y_i)-f(y_i))} + dx(c(x_i),\ f(y_i))\frac{(x_i-f(x_i))(c(y_i)-y_i)}{(c(x_i)-f(x_i))(c(y_i)-f(y_i))}$$
$$+ dx(f(x_i),\ c(y_i))\frac{(c(x_i)-x_i)(y_i-f(y_i))}{(c(x_i)-f(x_i))(c(y_i)-f(y_i))} + dx(c(x_i),\ c(y_i))\frac{(x_i-f(x_i))(y_i-f(y_i))}{(c(x_i)-f(x_i))(c(y_i)-f(y_i))}, \quad \text{(A1)}$$

$$y_{i+1} = y_i + dy(f(x_i),\ f(y_i))\frac{(c(x_i)-x_i)(c(y_i)-y_i)}{(c(x_i)-f(x_i))(c(y_i)-f(y_i))} + dy(c(x_i),\ f(y_i))\frac{(x_i-f(x_i))(c(y_i)-y_i)}{(c(x_i)-f(x_i))(c(y_i)-f(y_i))}$$
$$+ dy(f(x_i),\ c(y_i))\frac{(c(x_i)-x_i)(y_i-f(y_i))}{(c(x_i)-f(x_i))(c(y_i)-f(y_i))} + dy(c(x_i),\ c(y_i))\frac{(x_i-f(x_i))(y_i-f(y_i))}{(c(x_i)-f(x_i))(c(y_i)-f(y_i))}. \quad \text{(A2)}$$

[a]Author to whom correspondence should be addressed. Electronic mail: tvarghese@wisc.edu; Telephone: (608) 265-8797; Fax: (608) 262-2413.

[1]K. D. Kochanek, J. Xu, S. L. Murphy, and A. M. Miniño, "National Vital Statistics Reports Deaths : Preliminary Data for 2009," Statistics **59**, 5–38 (2011).
[2]V. L. Roger, A. S. Go, D. M. Lloyd-Jones, R. J. Adams, J. D. Berry, T. M. Brown, M. R. Carnethon, S. Dai, G. de Simone, E. S. Ford, C. S. Fox, H. J. Fullerton, C. Gillespie, K. J. Greenlund, S. M. Hailpern, J. A. Heit, P. M. Ho, V. J. Howard, B. M. Kissela, S. J. Kittner, D. T. Lackland, J. H. Lichtman, L. D. Lisabeth, D. M. Makuc, G. M. Marcus, A. Marelli, D. B. Matchar, M. M. McDermott, J. B. Meigs, C. S. Moy, D. Mozaffarian, M. E. Mussolino, G. Nichol, N. P. Paynter, W. D. Rosamond, P. D. Sorlie, R. S. Stafford, T. N. Turan, M. B. Turner, N. D. Wong, and J. Wylie-Rosett, "Heart disease and stroke statistics–2011 update: A report from the American Heart Association," Circulation **123**, e18–e209 (2011).
[3]V. Kotsis, S. Stabouli, I. Karafillis, S. Papakatsika, Z. Rizos, S. Miyakis, S. Goulopoulou, G. Parati, and P. Nilsson, "Arterial stiffness and 24h ambulatory blood pressure monitoring in young healthy volunteers: The early vascular ageing Aristotle University Thessaloniki Study (EVA-ARIS Study)," Atherosclerosis **219**(1), 194–199 (2011).
[4]M. F. O'Rourke, J. A. Staessen, C. Vlachopoulos, D. Duprez, and G. E. Plante, "Clinical applications of arterial stiffness; definitions and reference values," Am. J. Hypertens. **15**, 426–444 (2002).
[5]N. M. van Popele, D. E. Grobbee, M. L. Bots, R. Asmar, J. Topouchian, R. S. Reneman, A. P. G. Hoeks, D. A. M. van der Kuip, A. Hofman, and J. C. M. Witteman, "Association between arterial stiffness and atherosclerosis: The Rotterdam study," Stroke **32**, 454–460 (2001).
[6]D. S. Freedman, Z. Mei, S. R. Srinivasan, G. S. Berenson, and W. H. Dietz, "Cardiovascular risk factors and excess adiposity among overweight children and adolescents: the Bogalusa Heart Study," J. Pediatr. **150**, 12–17.e2 (2007).
[7]J. L. Cavalcante, J. A. C. Lima, A. Redheuil, and M. H. Al-Mallah, "Aortic stiffness: Current understanding and future directions," J. Am. Coll. Cardiol. **57**, 1511–1522 (2011).
[8]A. Redheuil, W.-C. Yu, C. O. Wu, E. Mousseaux, A. de Cesare, R. Yan, N. Kachenoura, D. Bluemke, and J. A. C. Lima, "Reduced ascending aortic strain and distensibility: earliest manifestations of vascular aging in humans," Hypertension **55**, 319–326 (2010).
[9]F. U. S. Mattace-Raso, T. J. M. van der Cammen, A. Hofman, N. M. van Popele, M. L. Bos, M. A. D. H. Schalekamp, R. Asmar, R. S. Reneman, A. P. G. Hoeks, M. M. B. Breteler, and J. C. M. Witteman, "Arterial stiffness and risk of coronary heart disease and stroke: the Rotterdam Study," Circulation **113**, 657–663 (2006).
[10]N. Ito, M. Ohishi, T. Takagi, M. Terai, A. Shiota, N. Hayashi, H. Rakugi, and T. Ogihara, "Clinical usefulness and limitations of brachial-ankle pulse wave velocity in the evaluation of cardiovascular complications in hypertensive patients," Hypertens. Res. **29**, 989–995 (2006).
[11]C. Stefanadis, C. Stratos, C. Vlachopoulos, S. Marakas, H. Boudoulas, I. Kallikazaros, E. Tsiamis, K. Toutouzas, L. Sioros, and P. Toutouzas, "Pressure-diameter relation of the human aorta: A new method of determination by the application of a special ultrasonic dimension catheter," Circulation **92**, 2210–2219 (1995).
[12]E. Hermeling, K. D. Reesink, L. M. Kornmann, R. S. Reneman, and A. P. Hoeks, "The dicrotic notch as alternative time-reference point to measure local pulse wave velocity in the carotid artery by means of ultrasonography," J. Hypertens. **27**, 2028–2035 (2009).
[13]J. Luo, R. Li, and E. Konofagou, "Pulse wave imaging of the human carotid artery: an in vivo feasibility study," IEEE Trans. Ultrason. Ferroelectr. Freq. Control **59**, 174–181 (2012).
[14]A. Kablak-Ziembicka, T. Przewlocki, W. Tracz, P. Pieniazek, P. Musialek, I. Stopa, J. Zalewski, and K. Zmudka, "Diagnostic value of carotid intima-media thickness in indicating multi-level atherosclerosis," Atherosclerosis **193**, 395–400 (2007).
[15]L. E. Chambless, G. Heiss, A. R. Folsom, W. Rosamond, M. Szklo, A. R. Sharrett, and L. X. Clegg, "Association of coronary heart disease incidence with carotid arterial wall thickness and major risk factors: The Atherosclerosis Risk in Communities (ARIC) Study, 1987–1993," Am. J. Epidemiol. **146**, 483–494 (1997).
[16]A. R. Folsom, R. A. Kronmal, R. C. Detrano, H. Daniel, O. Leary, D. E. Bild, D. A. Bluemke, M. J. Budoff, K. Liu, S. Shea, M. Szklo, and R. P. Tracy, "NIH Public Access," Epidemiology **168**, 1333–1339 (2008).
[17]J. H. Stein, C. E. Korcarz, and W. S. Post, "Use of carotid ultrasound to identify subclinical vascular disease and evaluate cardiovascular disease risk: Summary and discussion of the American Society of Echocardiography Consensus Statement," Prev. Cardiol. **12**, 34–38 (2009).
[18]J. Ophir, "Elastography: A quantitative method for imaging the elasticity of biological tissues," Ultrason. Imaging **13**, 111–134 (1991).
[19]T. Varghese, "Quasi-static ultrasound elastography," Ultrasound Clin. **4**, 323–338 (2009).
[20]T. Varghese, J. Ophir, E. Konofagou, F. Kallel, and R. Righetti, "Tradeoffs in elastographic imaging," Ultrason. Imaging **23**, 216–248 (2001).
[21]P. Chaturvedi, M. F. Insana, and T. J. Hall, "2D companding for noise reduction in strain imaging," IEEE Trans. Ultrason. Ferroelectr. Freq. Control **45**, 179–191 (1998).
[22]J. Jiang and T. J. Hall, "A parallelizable real-time motion tracking algorithm with applications to ultrasonic strain imaging," Phys. Med. Biol. **52**, 3773–3790 (2007).
[23]C. Pellot-Barakat, F. Frouin, M. F. Insana, and A. Herment, "Ultrasound elastography based on multiscale estimations of regularized displacement fields," IEEE Trans. Med. Imaging **23**, 153–163 (2004).
[24]P. N. T. Wells and H.-D. Liang, "Medical ultrasound: Imaging of soft tissue strain and elasticity," J. R. Soc., Interface **8**, 1521–1549 (2011).
[25]H. Shi, C. Mitchell, and M. McCormick, "Preliminary in vivo atherosclerotic carotid plaque characterization using the accumulated axial strain and relative lateral shift strain indices," Phys. Med. **53**, 6377–6394 (2008).
[26]H. Shi and T. Varghese, "Two-dimensional multi-level strain estimation for discontinuous tissue," Phys. Med. Biol. **52**, 389–401 (2007).
[27]R. L. Maurice, J. Ohayon, Y. Frétigny, M. Bertrand, G. Soulez, and G. Cloutier, "Noninvasive vascular elastography: Theoretical framework," IEEE Trans. Med. Imaging **23**, 164–180 (2004).
[28]H. Ribbers, R. G. P. Lopata, S. Holewijn, G. Pasterkamp, J. D. Blankensteijn, and C. L. de Korte, "Noninvasive two-dimensional strain imaging of arteries: Validation in phantoms and preliminary experience in carotid arteries in vivo," Ultrasound Med. Biol. **33**, 530–540 (2007).
[29]D. Dumont, R. H. Behler, T. C. Nichols, E. P. Merricks, and C. M. Gallippi, "ARFI imaging for noninvasive material characterization of atherosclerosis," Ultrasound Med. Biol. **32**, 1703–1711 (2006).
[30]W. M. Suh, A. H. Seto, R. J. P. Margey, I. Cruz-Gonzalez, and I.-K. Jang, "Intravascular detection of the vulnerable plaque," Circulation **4**, 169–178 (2011).
[31]G. E. Trahey, M. L. Palmeri, R. C. Bentley, and K. R. Nightingale, "Acoustic radiation force impulse imaging of the mechanical properties of arteries: In vivo and ex vivo results," Ultrasound Med. Biol. **30**, 1163–1171 (2004).
[32]R. H. Behler, T. C. Nichols, H. Zhu, E. P. Merricks, and C. M. Gallippi, "ARFI imaging for noninvasive material characterization of atherosclerosis. Part II: Toward in vivo characterization," Ultrasound Med. Biol. **35**, 278–295 (2009).
[33]P. E. Barbone and J. C. Bamber, "Quantitative elasticity imaging: what can and cannot be inferred from strain images," Phys. Med. Biol. **47**, 2147–2164 (2002).
[34]J. F. Granada, K. Milewski, H. Zhao, J. J. Stankus, A. Tellez, M. S. Aboodi, G. L. Kaluza, C. G. Krueger, R. Virmani, L. B. Schwartz, and A. Nikanorov, "Vascular response to zotarolimus-coated balloons in injured superficial femoral arteries of the familial hypercholesterolemic swine," Circulation **4**, 447–455 (2011).

[35]A. F. L. Schinkel, C. G. Krueger, A. Tellez, J. F. Granada, J. D. Reed, A. Hall, W. Zang, C. Owens, G. L. Kaluza, D. Staub, B. Coll, F. J. Ten Cate, and S. B. Feinstein, "Contrast-enhanced ultrasound for imaging vasa vasorum: comparison with histopathology in a swine model of atherosclerosis," Eur. J. Echocardiogr. **11**, 659–664 (2010).

[36]A. Tellez, C. G. Krueger, P. Seifert, D. Winsor-Hines, C. Piedrahita, Y. Cheng, K. Milewski, M. S. Aboodi, G. Yi, J. C. McGregor, T. Crenshaw, J. D. Reed, B. Huibregtse, G. L. Kaluza, and J. F. Granada, "Coronary bare metal stent implantation in homozygous LDL receptor deficient swine induces a neointimal formation pattern similar to humans," Atherosclerosis **213**, 518–524 (2010).

[37]J. Hasler-Rapacz, H. Ellegren, A. K. Fridolfsson, B. Kirkpatrick, S. Kirk, L. Andersson, and J. Rapacz, "Identification of a mutation in the low density lipoprotein receptor gene associated with recessive familial hypercholesterolemia in swine," Am. J. Med. Genet. **76**, 379–386 (1998).

[38]J. Hasler-Rapacz, H. J. Kempen, H. M. Princen, B. J. Kudchodkar, A. Lacko, and J. Rapacz, "Effects of simvastatin on plasma lipids and apolipoproteins in familial hypercholesterolemic swine," Arterioscler., Thromb., Vasc. Biol. **16**, 137–143 (1996).

[39]J. Hasler-Rapacz, M. F. Prescott, J. Von Linden-Reed, J. M. Rapacz, Z. Hu, and J. Rapacz, "Elevated concentrations of plasma lipids and apolipoproteins B, C-III, and E are associated with the progression of coronary artery disease in familial hypercholesterolemic swine," Arterioscler., Thromb., Vasc. Biol. **15**, 583–592 (1995).

[40]J. O. Hasler-Rapacz, T. C. Nichols, T. R. Griggs, D. A. Bellinger, and J. Rapacz, "Familial and diet-induced hypercholesterolemia in swine. Lipid, ApoB, and ApoA-I concentrations and distributions in plasma and lipoprotein subfractions," Arterioscler., Thromb., Vasc. Biol. **14**, 923–930 (1994).

[41]R. Wernersson, M. H. Schierup, F. G. Jørgensen, J. Gorodkin, F. Panitz, H.-H. Staerfeldt, O. F. Christensen, T. Mailund, H. Hornshøj, A. Klein, J. Wang, B. Liu, S. Hu, W. Dong, W. Li, G. K. S. Wong, J. Yu, J. Wang, C. Bendixen, M. Fredholm, S. Brunak, H. Yang, and L. Bolund, "Pigs in sequence space: a 0.66X coverage pig genome survey based on shotgun sequencing," BMC Genomics **6**, 70 (2005).

[42]A. D. Attie, R. J. Aiello, and W. J. Checovich, *The Spontaneously Hypercholesterolemic Pig as an Animal Model of Human Hypercholesterolemia*, 1st ed. (Iowa State College, Ames, 1992).

[43]M. E. Tumbleson, *Swine in Biomedical Research* (Plenum, New York 1986), Vol. 1.

[44]W. G. Pond, *Nutrition and Cardiovascular System of Swine* (CRC, Boca Raton, FL, 1986), Vol. 2.

[45]L. Chen, G. M. Treece, J. E. Lindop, A. H. Gee, and R. W. Prager, "A quality-guided displacement tracking algorithm for ultrasonic elasticity imaging," Med. Image Anal. **13**, 286–96 (2009).

[46]C. L. de Korte, E. I. Céspedes, A. F. van der Steen, and C. T. Lancée, "Intravascular elasticity imaging using ultrasound: Feasibility studies in phantoms," Ultrasound Med. **23**, 735–746 (1997).

[47]A. Gnasso, C. Carallo, C. Irace, V. Spagnuolo, G. De Novara, P. L. Mattioli, and A. Pujia, "Association between intima-media thickness and wall shear stress in common carotid arteries in healthy male subjects," Circulation **94**(12), 3257–3262 (1996).